batteries

MDPI

Formatted

*Article*

# Hydrogen storage characteristics and corrosion behavior of ~~$Ti_{34}V_{40}Cr_{24}Fe_2$~~ $Ti_{24}V_{40}Cr_{34}Fe_2$ alloy

**Jimoh Mohammed Abdul [1,2*], Lesley Hearth Chown [1], Jamiu K. Odusote [3], Jean Nei [4], Kwo-Hsiung Young [4] and Woli Taiye Olayinka[2]**

[1] School of Chemical and Metallurgical Engineering, Faculty of Engineering and Built Environment, University of the Witwatersrand, Johannesburg Private Bag 3, Wits 2050, South Africa; ~~XXX~~Lhchown@gmail.com (L.H.C);
[2] Department of Mechanical Engineering, Faculty of Engineering, Federal Polytechnic, Offa, Nigeria~~; XXX~~
[3] Department of Metallurgy and Material ~~Science~~Engineering, Faculty of Engineering University of Ilorin, Nigeria; ~~XXX~~jamiukolawole@gmail.com (J.K.O.);
[4] BASF/Battery Materials-Ovonic, 2983 Waterview Drive, Rochester Hills, MI 48309, USA; jean.nei@basf.com (J.N.); kwo.young@basf.com (K.Y)
* Correspondence: jmabdul@gmail.com; jmabdul66@yahoo.com; Tel.: +1-234-805-562-9924; +234-090-848-80106

Academic Editor: XXX
Received: date; Accepted: date; Published: date

**Abstract:** In this work, we investigated the effects of heat treatment on the microstructure, hydrogen storage characteristics and corrosion rate of a $Ti_{34}V_{40}Cr_{24}Fe_2$ alloy. The arc melted alloy was divided into three samples, two of which were separately quartz-sealed under vacuum and heated to 1000 °C for 1 h; one of these samples was quenched and the other furnace cooled to ambient temperature. The crystal structures of the samples were studied via X-ray diffractometry and scanning electron microscopy. Hydrogenation/dehydrogenation characteristics were investigated using a Sievert apparatus. Potentiostat corrosion tests on the alloys were performed using an AutoLab® corrosion test apparatus and electrochemical cell. All samples exhibited a ~~mixture of~~major body-center-cubic (BCC) and ~~α-Ti~~ some secondary phases. Abundance of Laves phases found in the as-cast sample reduced with annealing and disappeared in the quenched sample. Beside suppressing Laves phase ~~structures~~, annealing also introduced a Ti-rich phase. The corrosion rate, maximum absorption, and useful capacities increased after both heat treatments. The annealed sample had the highest absorption and reversible capacity. The plateau pressure of the as-cast alloy increased after quenching. The corrosion rate increased from 0.0004 mm/y in as-cast sample to 0.0009 mm/y after annealing and 0.0017 mm/y after quenching~~, due to a decrease in the Cr content of the C14 phase~~.

**Keywords:** Ti-V-Cr-Fe alloy; hydrogen storage characteristics; metal corrosion; heat treatment; crystal structure

## 1. Introduction

Ti-V-Cr body-centered-cubic (BCC) solid solution alloys are very promising to store a large quantity of hydrogen at room temperature [1–3]. Some of the identified shortcomings of these alloys include poor pressure-composition-temperature (PCT) plateau characteristics, low hydrogen desorption capacities, and long activation times [4–7]. In an attempt to improve on these shortcomings, controlled quantities of additives such as Fe, Zr and Mn have been found to be effective in lowering cost and enhancing the overall performance of the alloy [8–11]. The effects of substituting Fe for Cr on the hydrogen storage property of the $Ti_{0.32}Cr_{0.43}V_{0.25}$ alloy showed that desorption plateau pressure increased without decrease in effective hydrogen capacity suggesting possibility of using

Formatted

ferrovanadium as a substitute for the expensive pure vanadium [12]. Increasing the V content in $V_x$–$(Ti–Cr–Fe)_{100-x}$ (Ti/(Cr+Fe) = 1.0, Cr/Fe = 2.5, $x$ = 20–55) alloys lead to increase in both the hydrogen absorption capacity and desorption capacity but decreased the plateau pressure [13]. Miao *et al* [14]. found that all of the alloys $Ti_{0.8}Zr_{0.2}V_{2.7}Mn_{0.5}Cr_{0.8-x}Ni_{1.25}Fe_x$(x = 0.0 -0.8) mainly consist of two phases, the C14 Laves phase with three-dimensional network and the dendritic V-based solid solution phase. Further, the lattice parameters of the two phases and the maximum discharge capacity decrease with increase in Fe content but the cyclic stability and the high rate dischargeability increase firstly and then decrease with increasing $x$. Liu *et al.* [15] found that Ce addition favors the chemical homogeneity of the BCC phase and, therefore, improves the hydrogen storage properties of the $(Ti_{0.267}Cr_{0.333}V_{0.40})_{93}Fe_7Ce_x$ ($x$ = 0, 0.4, 1.1 and 2.0 at%) alloys. To increase the hydrogen storage capacity and the plateau pressure of the $Ti_{0.32}Cr_{0.43}V_{0.25}$ alloy, Yoo *et al.* [16] replaced a fraction of the Cr with Mn or a combination of Mn and Fe. When Mn was used alone, the effective hydrogen storage capacity increased to about 2.5 wt% though the plateau pressure showed no significant change. However when Fe was added with Mn, both the effective hydrogen storage capacity and the plateau pressure increased.

Further efforts include assessing the effects of heat treatment on hydrogen absorption properties; Okada *et al*. [17] found that moderate heat treatment, specifically annealing at 1573 K for 1 min, enhances the storage capacity and flattens the desorption plateau of $Ti_{25}Cr_{40}V_{35}$ alloy. Liu *et al*. [18] reported that heat treatment effectively improves the flatness of plateau and improves the hydrogenation capacity of $Ti_{32}Cr_{46}V_{22}$ alloy by lowering the oxygen concentration and homogenizing the composition and microstructure. A hydrogen desorption capacity of 2.3 wt% was achieved when $Ti_{32}Cr_{40}V_{25}$ was annealed at 1653 K for 1 min. [19]. Chuang *et al*. [20] found that annealing atomized powder of Ti-Zr based alloy at 1123 K for 4 h greatly enhanced the discharge capacity. Hang *et al*. [21] heat treated $Ti_{10}V_{77}Cr_6Fe_6Zr$ alloy at a relatively lower temperature, but elongated the soaking time by annealing at 1523 K for 5 min and at 1373 K for 8 h and found that sample annealed at 1523 K for 5 min has the best overall hydrogen storage properties, with a desorption capacity of 1.82 wt% and a dehydriding plateau pressure of 0.75 MPa.

Although BCC solid solution alloys have very high gaseous phase hydrogen storage capacities, they suffer from the severe capacity degradation during electrochemical applications due to leaching-out of Vanadium (V) into the KOH electrolyte [22, 23]. The preferential leaching of V in the negative electrode material has been previously identified [24] and V-free Laves phase alloys have been adopted to mitigate the consequent cycle life and self-discharge issues originating from V-corrosion [25,26].

Metal corrosion mainly occurs through electrochemical reactions at the interface between the metal and electrolyte [27]. The basic process of metallic corrosion in aqueous solution consists of the anodic dissolution of metals and the cathodic reduction of oxidants present in the solution:

$M_m \rightarrow M^{2+}_{aq} + 2e^-_m$ anodic oxidation

$2Ox_{aq} + 2e^-_m \rightarrow 2Red(e^-_{redox})_{aq}$ cathodic oxidation

In the formulae, $M_m$ is the metal in the state of metallic bonding, $M^{2+}_{aq}$ is the hydrated metal ion in aqueous solution, $e^-_m$ is the electron in the metal, $Ox_{aq}$ is an oxidant, $Red(e^-_{redox})_{aq}$ is a reductant, and $e^-_{redox}$ is the redox electron in the reductant. The overall corrosion reaction is then written as follows:

$M_m + 2Ox_{aq} \rightarrow M^{2+}_{aq} + 2Red(e^-_{redox})_{aq}$

These reactions are charge-transfer processes that occur across the interface between the metal and the aqueous solution, hence they are dependent on the interfacial potential that essentially corresponds to what is called the electrode potential of metals in electrochemistry terms. In physics terms, the electrode potential represents the energy level of electrons, called the Fermi level, in an electrode immersed in electrolyte. For normal metallic corrosion, in practice, the cathodic process is carried out by the reduction of hydrogen ions and/or the reduction of oxygen molecules in aqueous

solution. These two cathodic reductions are electron transfer processes that occur across the metal–solution interface, whereas anodic metal dissolution is an ion transfer process across the interface.

The rate of the reaction is evaluated in terms of the corrosion current. The natural logarithm of the absolute value of the corrosion current versus potential is plotted as a Tafel curve. The corrosion current values can be transformed to corrosion rate (*CR*) values (e.g. mm/y) using Equation 1 [28]:

$$CR = K \frac{i_{corr}}{\rho} EW, \quad (1)$$

where $K$ is a constant that depends on the unit of corrosion rate; $K$ = 3272 for mm/y (mmpy), or = 1.288 x $10^5$ for milli-inches/y (mpy), $i_{corr}$ = corrosion current density, (μA $Cm^{-2}$), $\rho$ = alloy density. ($g\ Cm^{-3}$), $EW$ = Equivalent weight = 1/electron equivalent (Q) where:

$$Q = \sum \frac{n_i f_i}{W_i}, \quad (2)$$

where $n_i$ = the valence if $i^{th}$ element of the alloy, $f_i$ = the mass fraction of the $i^{th}$ element in the alloy, W$i$ = the atomic weight of the $i^{th}$ element in the alloy.

By combining Equations 1 and 2, the penetration rate (*CR* and mass loss, *ML*) of an alloy is given by:

$$CR = K_1 \frac{i_{corr}}{\rho \sum \frac{n_i f_i}{W_i}} \quad (3)$$

$$ML = K_2 i_{corr} EW \quad (4)$$

The equations above give values of 0.1288 if the unit of CR is m/y and 0.03272 if the unit of CR is mm/y [27]. This work investigates the influence of heat treatment on hydrogen storage capacity and corrosion rate of $Ti_{34}V_{40}Cr_{24}Fe_2$ in standard KOH electrolyte. V-based hydrogen storage alloys are often used as the anode in NiMH batteries [29].

Cho et al [30] identified a composition region in the Ti-V-Cr phase diagram as having the highest hydrogen uptake. This informed the choice of the base alloy $Ti_{25}V_{40}Cr_{35}$, which falls within the region. Choice of Fe additive was made because of its relatively cheap cost. Literature showed that in the ternary Ti-V-Cr system [12-16,31], Fe substituted Cr or V and FeV used in place of expensive V. Thereby creating a research gap of not investigating effect of substituting Fe at Ti site on hydrogen storage and corrosion behavior of $Ti_{25}V_{40}Cr_{35}$. The present work on substituting equal quantity of Fe for Cr and Ti on the hydrogen storage and corrosion behavior of $Ti_{25}V_{40}Cr_{35}$ therefore fills the gap.

## 2. Experimental Setup

The raw materials for this work were sourced from Metrohm South Africa. Iron (325-290 mesh, 99% purity, 0.01% C and 0.015% P and S); chromium (<0.3mm, 99.8% purity) vanadium (-325 mesh, 99.5% purity), titanium (-325 mesh, 99.5% purity). 10g sample of $Ti_{34}V_{40}Cr_{24}Fe_2$ alloy was prepared in a water-cooled, copper-crucible arc melting furnace under argon atmosphere. The ingot was turned over and remelted three times to ensure homogeneity. After melting, the ingot was divided into three pieces. Two cut samples were vacuum-sealed in separate silica glass tubes in preparation for heat treatment.

The two quartz-sealed specimens were loaded in a heat treatment furnace and heated to 1000 °C for 1 h. One tube was immediately removed and broken in cold water to quench the alloy,thereby locking the microstructure, while the second sample was slowly furnace-cooled to room temperature.

Crystal structure and lattice parameters in the as-cast and heat-treated samples were determined by X-ray diffraction (XRD) analysis, using a Bruker D2_Phaser X-ray® diffraction instrument (Bruker AXS, Inc., Madison, Wisconsin, USA) with Cu-$K_\alpha$ radiation from 2θ = 10° to 80°. Xpert High Score® phase identification software produced by Philips analytical B.V. Almelo Netherlands was used to identify the phases from the XRD data. Elemental compositions of the phases were determined using

a FEI Nova NanoSEM 200® scanning electron microscope (SEM) (FEI, Hillsboro, Oregon, USA) fitted with EDAX® advanced microanalysis solution (EDAX Inc., Mahwah, New Jersey, USA). The amount of the phases was determined by image analysis using the ImageJ freeware (National Institute of Mental Health, Bethesda, Maryland, USA).

Pottentiostatic corrosion tests on the alloys were performed using an AutoLab® corrosion test apparatus (Metrohm Autolab B.V., Utrecht, The Netherlands) and an electrochemical cell consisting of a tri-electrode; platinum reference electrode, Ag/AgCl counter electrode, and 0.14 $cm^2$ test alloy as the working electrode; aqueous solution of 6 mol $L^{-1}$ KOH was used as the electrolyte. The alloys were cut into rectangles and a copper wire of suitable length was attached to one side of the specimen with aluminum tape. The sample was then covered in cold-resin for 24 h to enable curing, while leaving only the test surface exposed. When cured, the test surface was ground to 1200 grit. The corrosion experiments were performed at 25 °C and Tafel curves were recorded from –1.4V to –0.2 V with a scanning rate of 1 mV $sec^{-1}$.

Measurement of the PCT isotherms was performed using a Suzuki-Shokan multi-channel PCT (Suzuki Shokan, Tokyo, Japan) system. Samples were crushed into particles < 75 μm in size and 1g of each alloy was sealed into a stainless steel reactor and heated to 573 K. Next, 3 MPa of Hydrogen pressure was introduced into the apparatus for 30 min, followed by slow cooling to room temperature in a hydrogen atmosphere. The alloys absorbed most of the hydrogen and were pulverized in this step. After the hydrogenation process, the samples were heated to 573 K and chamber was evacuated for 1 h with a mechanical pump to completely dehydrogenate the samples for PCT measurements at 303, 333, and 363 K successively.

Formatted

## 3. Results and discussion

### *3.1. Microstrcuture*

~~The XRD pattern in Figure 1 showed that the primary light grey phase corresponds to the main peak of BCC (V) phase, while the black intergranular and the dark phases were the minor peaks of the α-Ti phase. Table 1 showed that the proportion of the BCC (V) phase in as-cast sample was ~79% area-wise. The dark phase and light grey α-Ti phases made up approximately 20% and 1.3%, respectively, of the total alloy. Annealing had no effect on the composition of the BCC phase, but increased the proportion of BCC phase to 82%. Quenching reduced the proportion of BCC by 11% and increased Ti content by ~4 at%. Proportion of the α-Ti phase was slightly reduced from 20% in the as-cast sample to 18% in the annealed sample, but increased to 32.5% after quenching.~~

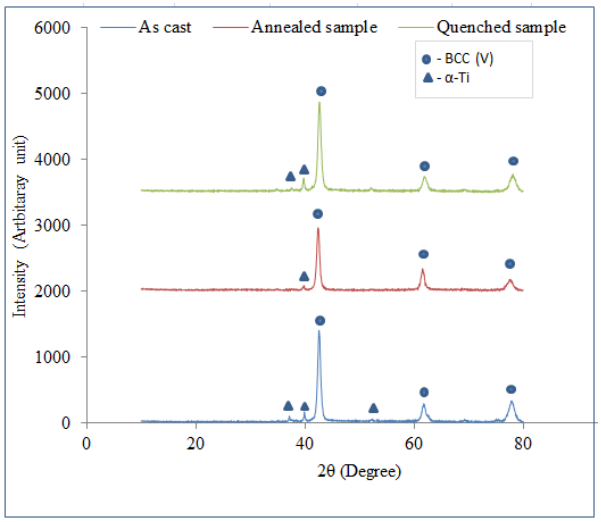


The XRD pattern in Figure 1 shows mainly a BCC (V) phase and some minor peaks from secondary phases. Phase analysis indicated both C14 and C15 phases co-existed in the as-cast sample and transformed into an α-Ti phase after annealing (Table 1). Changes in the lattice parameters of the

BCC main phase and the α -Ti secondary phase with the different preparation methods are negligible. Annealed sample showed the least amount of α-Ti.

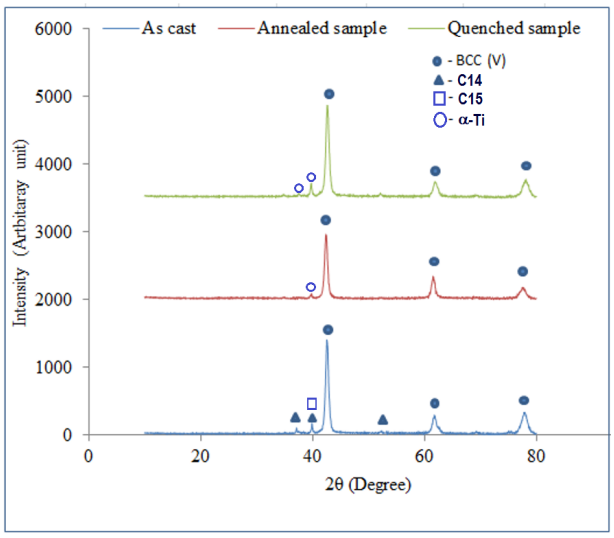


**Figure 1.** XRD patterns of as-cast and heat treated $Ti_{34}V_{40}Cr_{24}Fe_2$ alloys.

Formatted

**Table 1. XRD crystallographic parameters of as-cast and heat treated $Ti_{34}V_{40}Cr_{24}Fe_2$.**

| | | Crystallographic description | | | |
|---|---|---|---|---|---|
| **Sample** | **Phases** | **Space group (no.)** | ***a*** | ***c*** | **Unit cell volume ($Å^3$)** |
| As-cast | BCC (V) | $Im\bar{3}m$ (229) | 3.00 | | 27.08 |
| | C14 (Laves) | $P6_3/mmc$ (194) | 4.85 | 7.94 | 161.7 |
| | C15 (Laves) | $Fd\bar{3}m$ (227) | 6.943 | | 334.69 |
| Annealed | BCC (V) | $Im\bar{3}m$ (229) | 3.01 | | 27.37 |
| | α-Ti | $P6_3/mmc$ (194) | 2.98 | 4.73 | 36.24 |
| Quenched | BCC (V) | $Im\bar{3}m$ (229) | 3.01 | | 27.37 |
| | α-Ti | $P6_3/mmc$ (194) | 2.98 | 4.73 | 36.24 |

Formatted

Figure 2 shows representative back scattering electron (BSE) images of as-cast and heat treated (both slow cooled and quenched) $Ti_{34}V_{40}Cr_{24}Fe_2$. The microstructure of the alloy was a primary, light grey phase (C) with ~~a black intergranular phase (D) in all three samples. X-ray energy dispersive spectroscopy (EDS) analyses on the dark portions (E) on the micrographs of annealed samples have the same elemental compositions as those in the α Ti phase. Heat treatment removed the dark grey phase.~~some darker intergranular phases (D and E) in all three samples. The primary light grey phase corresponds to the main peak of BCC (V) phase, while the black intergranular and the dark phases were the Laves and Ti-rich secondary phases. X-ray energy dispersive spectroscopy (EDS) was used to measure compositions in the areas of interest and the results are summarized in Table 2. EDS technique measures the average composition within 1-2 microns volume (depending on the primary electron energy) due to the nature of electron scattering in the solid. The secondary phases in this study are either below or about that range and therefore EDS result can only indicate relative change in composition. In the as-cast sample, areas D and E have relatively higher Ti-contents with a smaller atomic weight, which resulting in a darker contrast. Areas D and E are assigned to C14 and C15 from

the combining results from XRD and EDS measurements. In the annealed sample, C15 phase transformed into C14 phase (area D) and a Ti-rich phase (area E) started to appear. We believe This Ti-rich phase can be assigned to the α-Ti phase found in XRD analysis. The α-Ti phase only has a very small solubility of Cr and V [32]. The high V and Cr-contents found in the EDS data in Table 2 can be explained by either a small grain size of Ti-phase which is below the sampling volume of the EDS technique or it is a mixture of microcrystalline of Ti/C15 happened as the product of a Eutectic solidification at 667 °C [32]. Quenching introduced twinning in the secondary phase, shown inside the circle (F). Addition of Fe into the TiVCr solid solution is known to promote the secondary Laves phase [~~32–34~~33–35], which is considered to be a catalyst that facilitates hydrogenation/dehydrogenation kinetics [~~35]~~.36]. Reduction in the ~~C14 secondary~~Laves phase abundance by thermal annealing was reported before with a Laves phase-related BCC TiZrV-based alloy [~~36~~37].

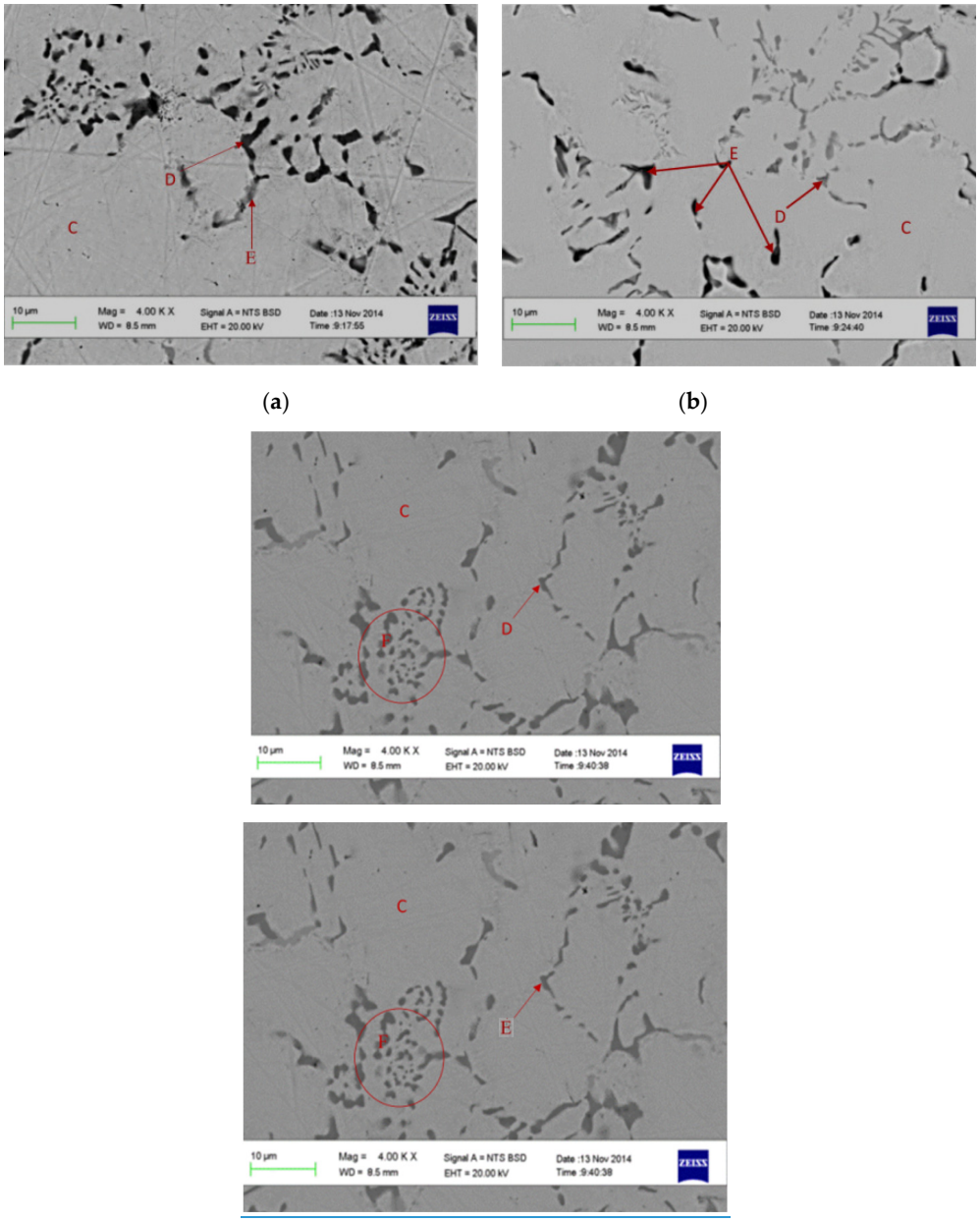


(**a**) (**b**)

(**c**)

**Figure 2.** SEM BSE micrographs of (**a**) as-cast, (**b**) annealed, and (**c**) quenched $Ti_{34}V_{40}Cr_{24}Fe_2$.

Formatted

Table ~~1~~2 showed that the BCC (V) in all the three samples contained 17–22 at% Ti, 40–44 at% V, and ~36 at% Cr. The black intergranular ~~α-Ti phase~~ E areas in Figure 2b and 2c contained 23–66 at%

Ti, 18–41 at% V, and 14–36 at% Cr. The heat treatment ~~removed~~reduced the ~~dark grey C14~~ Laves ~~(unit cell volume 161.7 Å³).~~phase abundance from 21.5 to 18 % and the quenching totally removed it. The Ti/Cr ratio in the BCC phase is almost equal in all three samples. However, the ratio of the ~~secondary~~darker areas (containing Laves phase and Ti-phase) increased from 0.6 to 4.4 after annealing and ~2 after quenching.

Formatted

**Table ~~1. EDX and crystallographic parameters~~2. EDS results of as-cast and heat treated $Ti_{34}V_{40}Cr_{24}Fe_2$.**

| Sample | ~~Phases XRD~~Location | Composition (at%) Ti | V | Cr | Fe | Ti/Cr ratio | ~~Phase proportion (% area)~~ Phase Identification | ~~Crystallographic description~~ ~~Space group (no.)~~ | ~~a~~ | ~~c~~ | ~~Unit cell vol. (Å³)~~ | Phase proportion (% area) |
|---|---|---|---|---|---|---|---|---|---|---|---|---|
| As-cast | ~~BCC (V)~~C | 17.7 (1.1) | 43.5 (1.6) | 36.5 (2.2) | 2.3 (0.7) | 0.5 | BCC | 78.5 | ~~$Im\bar{3}m$ (229)~~ | ~~3.00~~ | ~~27.08~~ | |
| | ~~α-Ti~~ | ~~23.0 (3.7)~~ | ~~41.4 (2.4)~~ | ~~35.5 (1.4)~~ | ~~2.0 (0.2)~~ | ~~0.6~~ | ~~20.2~~ | ~~$P6_3/mmc$ (194)~~ | ~~2.98~~ | ~~4.73~~ | ~~36.24~~ | |
| | ~~C14 (Laves)~~D | 24.7 (0.8) | 37.8 (0.7) | 34.0 (0.4) | 3.5 (0.3) | 0.7 | C14 | 1.3 | ~~$P6_3/mmc$ (194)~~ | ~~4.85~~ | ~~7.94~~ | ~~161.7~~ |
| | E | 23.0 (3.7) | 41.4 (2.4) | 35.5 (1.4) | 2.0 (0.2) | 0.6 | C15 | | 20.2 | | | |
| Annealed | ~~BCC (V)~~C | 17.7 (1.9) | 43.5 (1.3) | 36.5 (2.9) | 2.3 (0.2) | 0.5 | BCC | 82.0 | ~~$Im\bar{3}m$ (229)~~ | ~~3.01~~ | ~~27.37~~ | |
| | D | 25.3 (0.8) | 36.5 (0.7) | 33.8 (0.4) | 4.4 (0.3) | 0.7 | C14 | | 6.0 | | | |
| | ~~α-Ti~~E | 65.9 (5.2) | 18.6 (2.8) | 14.9 (2.2) | 0.6 (0.2) | 4.4 | ~~18.0~~α-Ti/BCC | ~~$P6_3/mmc$ (194)~~12.0 | ~~2.98~~ | ~~4.73~~ | ~~36.24~~ | |
| Quenched | ~~BCC (V)~~C | 21.8 (1.5) | 40.0 (1.3) | 35.6 (1.2) | 2.6 (1.7) | 0.6 | BCC | 80.5 | ~~$Im\bar{3}m$ (229)~~ | ~~3.01~~ | ~~27.37~~ | |
| | ~~α-Ti~~E | 47.3 (3.7) | 21.6 (2.5) | 24.7 (1.4) | 6.4 (0.5) | 1.9 | α-Ti/BCC | 19.5 | ~~$P6_3/mmc$ (194)~~ | ~~4.85~~ | ~~7.94~~ | ~~161.7~~ |

### 3.2 *Gaseous phase hydrogen storage*

Table ~~2~~3 shows that both heat treatment processes increased the reversible hydrogen storage capacity (RHSC), the capacity increased from 0.44 to 1.26 wt% after annealing and to 0.65 wt% in quenched sample. Literature indicates that annealing increases hydrogen capacity [13,14]. The BCC phase enhances hydrogen capacity [11, 22, 29]; increase in its unit cell volume implies the availability of more hydrogen absorption sites or spaces, leading to an increase in storage capacity. The Laves phase is detrimental to storage capacity [10, ~~37–39~~38–40], and alloys with larger Laves unit cell volumes or high Laves proportions are known to exhibit lower hydrogen capacity. Therefore, the observed increase in useful capacity after heat treatment was due to the increase in BCC unit cell volume. The ~~larger unit cell volume~~abundance of ~~the~~catalytic Laves phase in the as-cast sample ~~disappeared~~reduced after annealing; this suggests another reason for the higher hydrogen capacity observed in the annealed sample.

Table ~~2~~3 also shows that desorption plateau pressure reduced after annealing the alloy at 1000 ~~°C~~°C for 1 hour and rose after quenching. Specifically, the pressure of the desorption plateau decreased from 1.32 to 0.68 MPa after annealing and increased to 2.34 MPa after quenching. The plateau properties are affected by both the homogeneity and oxygen content in Ti-V based hydrogen storage alloys [10]. Inhomogeneity of microstructure can be minimized by heat treatment at higher temperatures for a short time [~~40~~41]. The observed reduction in plateau pressure after annealing suggests a homogenized microstructure; in addition, the sample was annealed in a vacuum-sealed quartz tube, thereby preventing oxygen intake. The quenched sample was exposed to oxygen in the

quenching medium; therefore, the rise in plateau pressure suggests the presence of a higher oxygen content.

**Table 23.** Effect of heat treatment on H storage properties of $Ti_{34}V_{40}Cr_{24}Fe_2$ alloy

| Sample | Absorption capacity (wt%) | Capacity remaining (wt%) | RHSC (wt%) | Plateau pressure (MPa) |
|---|---|---|---|---|
| As-cast | 0.86 | 0.42 | 0.44 | 1.32 |
| Annealed | 1.54 | 0.28 | 1.26 | 0.68 |
| Quenched | 1.04 | 0.39 | 0.65 | 2.34 |

In Figure 3a, the PCT isotherms for both the as-cast and heat treated alloys were steep, an indication of high plateau pressure. However, the isotherm for the annealed sample showed a flatter and wider plateau, indicating a reduction in plateau pressure, and the wider plateau indicating higher hydrogen capacity.

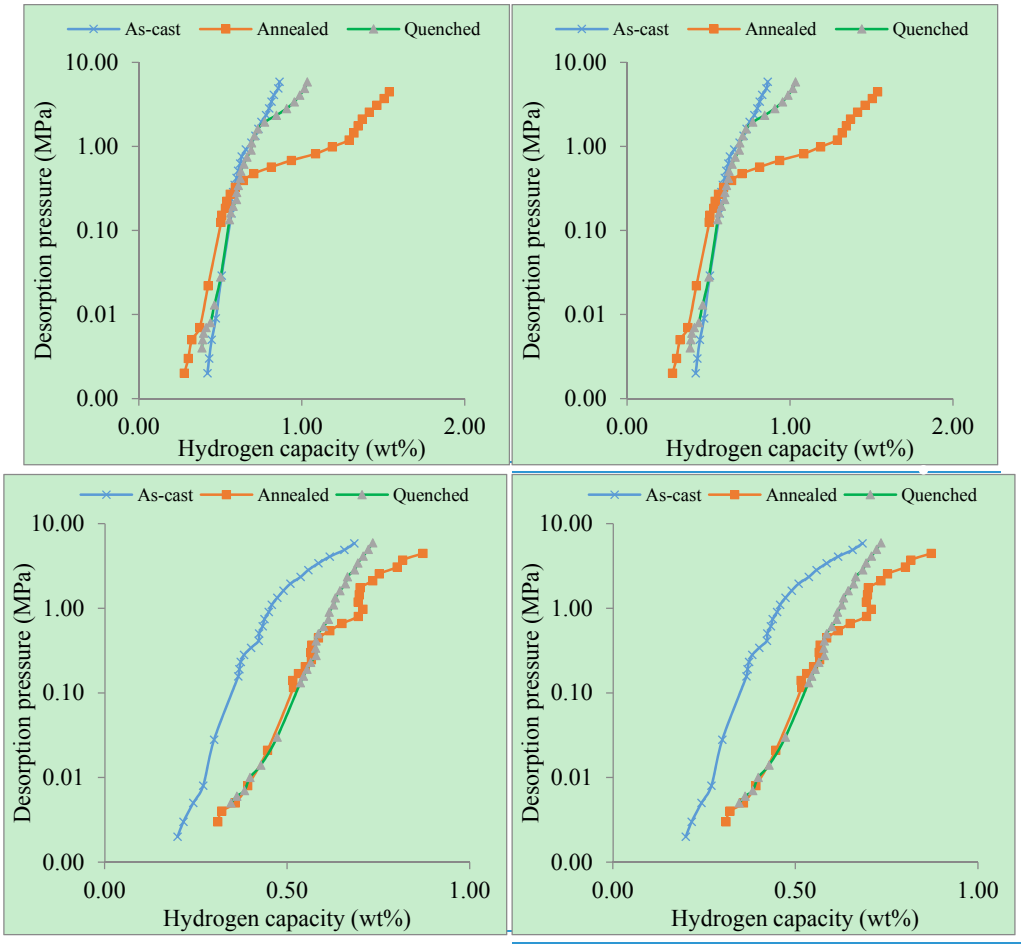


(a) (b)

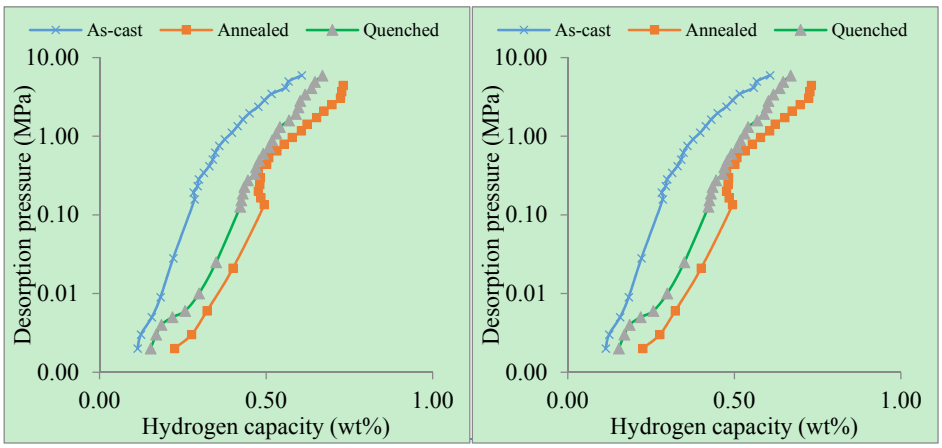


(c)

**Figure 3.** PCT desorption curves of the as-cast and heat treated $Ti_{34}V_{40}Cr_{24}Fe_2$ alloys at (**a**) 303, (**b**) 333, and (**c**) 363 K.

In Figure 4, the maximum absorption capacity decreased with increasing isotherm temperatures, similar to what has been previously described in the literature [~~41~~42]. For the as-cast sample, the maximum absorption capacity was 0.86 wt% at 30 °C, and the capacity declined to 0.69 and 0.62 wt% as the temperature rose to 333 and 363 K, respectively. Similar trends were observed for the annealed and quenched samples. Kinetic energy of gas increased with increasing temperatures; a low kinetic energy is associated with lower temperatures, while increased temperature leads to high kinetic energy. Hydrogen gas atoms with a low kinetic energy are more easily absorbed than those with high kinetic energy because gases with higher kinetic energy move faster, thus requiring additional force to attract to the surface of the adsorbate. This explains the observed higher capacity at low temperatures and lower capacity at high temperatures.

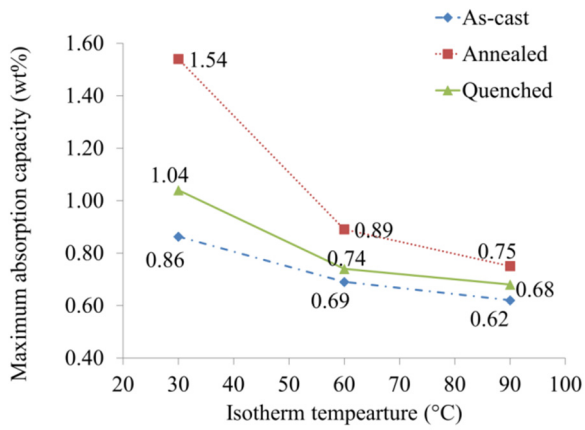


**Figure 4.** Influence of isotherm temperatures on maximum hydrogen capacity.

Stability of the current alloy can be improved with addition of Ni to promote other secondary phases, such as TiNi [~~42~~43] and $Ti_2Ni$ [~~43~~44]. The synergetic interaction between the main storage phase (BCC) and secondary phases can reduce the equilibrium plateau pressure of the BCC phase and make them available for electrochemical storage purpose [~~44~~45].

### *3.3 Corrosion behavior*

The corrosion behavior of $Ti_{34}V_{40}Cr_{24}Fe_2$ alloys in 30% KOH aqueous solution was studied by Tafel curve measurements and results are plotted in Figure 5a. No significant change was observed in corrosion potential ($E_{corr}$) for the as-cast alloy after annealing. However, a decrease from –0.80 to –0.867 mV was observed after quenching. Both heat treatment processes increased the corrosion rate

of the alloy (Figure 5b). The rate increased from 0.0004 in as-cast alloy to 0.0009 mm/y after annealing and to 0.0017mm/y after quenching.

Cr is known to improve the corrosion resistance of an alloy [~~45,~~ 46, 47]. Samples containing high at% Cr are expected to have low corrosion rates and vice versa. Therefore, an increase in the corrosion rate of heat treated samples could be a result of a reduction in Cr-content in the ~~C14~~ secondary phase. Phase structure and oxide layer are among the factors that determine the corrosion rate of an alloy. The Laves structure has been reported to have a thinner oxide layer than the BCC structure [~~47~~48] and this oxide layer is known for passivation of corrosion [~~48–50~~49–51]. It is therefore implied that for a dual phase alloy, like the alloys being investigated in this research, the corrosion rate will increase when the proportion of ~~α~~ Ti-rich phase with thinner oxide layer increases. The ~~α~~ Ti-rich phase is more easily corroded than the BCC phase [~~51]. The high α Ti phase proportion in the quenched sample therefore suggests the basis for the observed increase in corrosion rate.~~ 52].

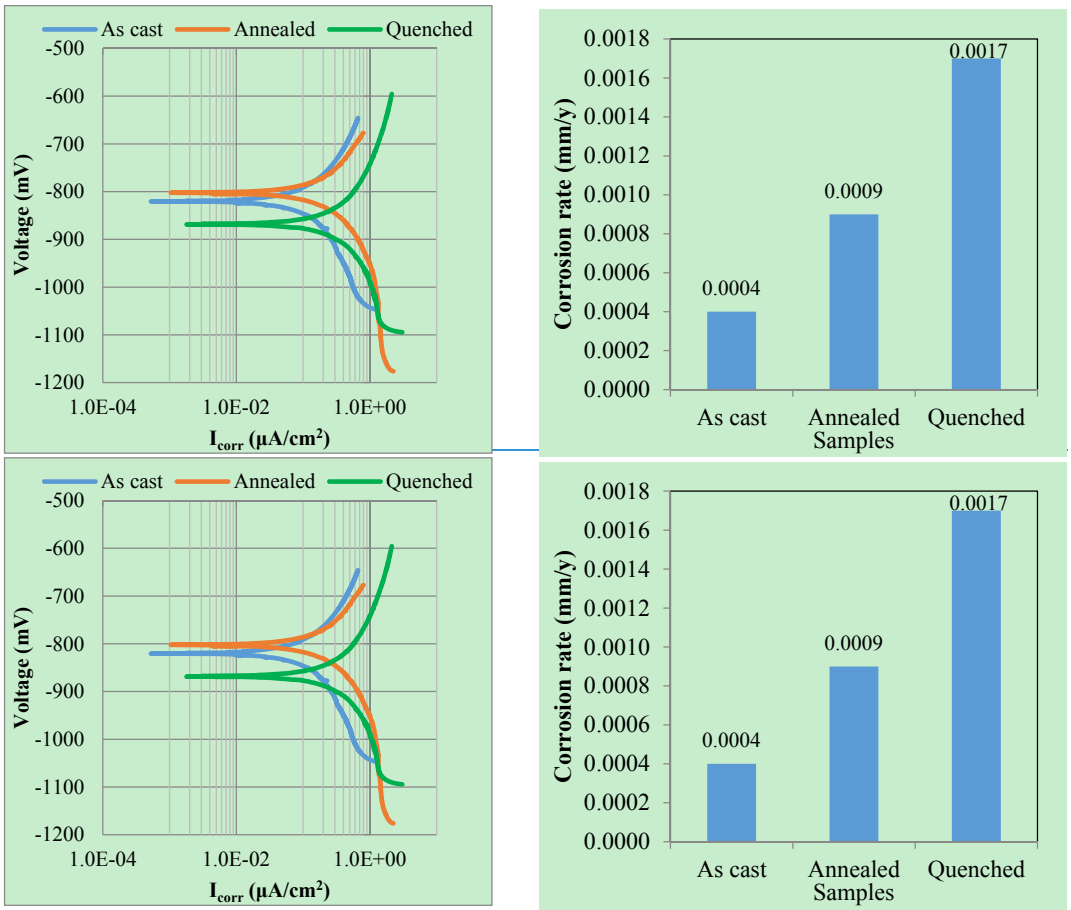


(**a**) (**b**)

**Figure 5.** (**a**) Tafel curves and (**b**) corrosion rates of the as-cast and heat treated $Ti_{34}V_{40}Cr_{24}Fe_2$.

## 4. Conclusions

The influence of heat treatment on the microstructure and hydrogen storage capacity of $Ti_{34}V_{40}Cr_{24}Fe_2$ at% alloys was investigated. ~~Both the as-cast and heat treated samples contained BCC and α Ti phases.~~The main phase of all alloys under different preparations is a BCC phase while the secondary phase shifted from Laves phase to a Ti-rich phase with annealing. Heat treatment was beneficial with regard to hydrogen capacity, but detrimental to corrosion behavior. Though both heat treatment processes enhanced useful hydrogen capacity, the annealed sample had superior storage characteristics. Although both annealing and quenching increased the corrosion rate of the alloy, the rate of corrosion was found to be highest in the quenched sample~~. For electrochemical applications,~~

~~annealing of a BCC-based metal hydride must be controlled in a manner that does not overly reduce the Cr-content in the C14 phase in order to minimize the corrosion rate~~ with the highest amount of Ti-rich phase.

**Acknowledgments:** The work is supported by African Material Science and Engineering Network, AMSEN, and the National Research Found NRF Thuthuka programme.

**Author Contributions:** Jimoh Mohammed Abdul and Lesley Hearth Chown designed the experiments and analyzed the results. Jamiu K. Odusote and Jean Nei conducted the corrosion and PCT measurements, respectively, and Kwo-Hsiung Young and Woli T. Olayinka, assisted in data analysis and manuscript preparation.

**Conflicts of Interest:** The authors declare no conflict of interest.

## Abbreviations

| | |
|---|---|
| BCC | Body-centered-cubic |
| PCT | Pressure-concentration-temperature |
| *CR* | Corrosion rate |
| $i_{corr}$ | Corrosion current density |
| *EW* | Equivalent weight |
| *ML* | Mass loss |
| XRD | X-ray diffractometer |
| SEM | Scanning electron microscopy |
| BSE | Back-scattering electron |
| EDS | Energy dispersive spectroscopy |
| RHSC | Reversible hydrogen storage capacity |
| $E_{corr}$ | Corrosion potential |

## References


1. Okada, M.; Kuriiwa, T.; Tamura, T.; Kamegawa, A. Ti-V-Cr b.c.c. alloys with high protium content. *J. Alloys Compd.* **2002**, *330–332*, 511–516.
2. Tamura, T.; Kazumi, T.; Kamegawa, A.; Takamura, H.; Okada M. Protium absorption properties and protide formations of Ti-Cr-V alloys. *J. Alloys Compd.* **2003**, *356–357*, 505–509.
3. Young, K.; Fetcenko, M.A.; Ouchi, T.; Im, J.; Ovshinsky, S.R.; Li, F.; Reinhout, M. Hydrogen Storage Materials Having Exunit cellent Kinetics, Capacity, and Cycle Stability. U.S. Patent 7,344,676, 18 March 2008.
4. Akiba, E.; H. Iba. Hydrogen absorption by Laves phase related BCC solid solution. *Intermetallics* **1998**, *6*, 461–470.
5. Cho, S.; Han, C.; Park, C.; Akiba, E. The hydrogen storage characteristics of Ti–Cr–V alloys. *J. Alloys Compd.* **1999**, *288*, 294–298.
6. Kuriwa, T.; Tamura, T.; Amemiya, T.; Fusa, T.; Kamegawa, A.; Takemura, T.; Okada, M. New V-based alloys with high protium absorption and desorption capacity. *J. Alloys Compd.* **1999**, *293–295* 433–436.
7. Seo, C.; Kim, J.; Lee, P.S.; Lee. J. Hydrogen storage properties of vanadium-based b.c.c. solid solution metal hydrides. *J. Alloys Compd.* **2003**, *348*, 252–257.
8. Tamura, T.; Tominaga, Y.; Matsumoto, K.; Fuda, T.; Kuriiwa, T.; Kamegawa, A.; Takamura, H.; Okada, M. Protium absorption properties of Ti-V-Cr-Mn alloys with a b.c.c. structure. *J. Alloys Compd.* **2002**, *330–332*, 522–525.
9. Huang, T.; Wu, Z,; Chen, J.; Yu, X.; Xia, B.; Xu, N. Dependence of hydrogen storage capacity of $TiCr_{1.8-x}(VFe)_x$ on V-Fe content. *Mat. Sci. Engineer. A.* **2004**, *385*, 17–21.
10. Yu, X.B.; Wu, Z.; Xia, B.J.; Xu, N.X. Enhancement of hydrogen storage capacity of Ti–V–Cr–Mn BCC phase alloys. *J. Alloys Compd.* **2004**, *372*, 272–277.
11. Hang, Z.; Xiao, X.; Tan, D.; He, Z.; Li, W.; Li, S.; Chen, C.; Chen, L. Microstructure and hydrogen storage properties of $Ti_{10}V_{84-x}Fe_6Zr_x$ (x = 1–8) alloys. *Int. J. Hydrogen Energy* **2010**, *35*, 3080–3086.
12. ~~Jeong HyunYooa, G.~~Yooa, J.; Shim, ~~S. W.~~G.; Cho, ~~and C. N.~~S.; Park, C. Effects of desorption temperature and substitution of Fe for Cr on the hydrogen storage properties of $Ti_{0.32}Cr_{0.43}V_{0.25}$ alloy. ~~International Journal of~~*Int. J. Hydrogen Energy* ~~–~~**2007**~~.~~, *32*~~: p.~~, 2977~~–~~2981.
13 ~~Yigang~~Yan, Y~~.,~~.; Chen, Y.; Liang, H.; Zhou, X.; Wu, C~~. Yungui, L. Hao, Z. Xiaoxiao, W. Chaoling, T. Mingda, and L.~~.; Tao, M.; Pang, L. Hydrogen storage properties of V–Ti–Cr–Fe alloys. ~~Journal of~~*J. Alloys* ~~and Compounds~~*Compd.* **2008**~~.~~., *454*~~(5): p.~~, 427~~–~~–431.
14 Miao H., ~~M.~~ Gao, ~~Y.~~M.; Liu, Y~~.~~.; Lin, ~~J.~~Y.; Wang, ~~and H.~~J.; Pan, H. Microstructure and electrochemical properties of Ti–V-based multiphase hydrogen storage electrode alloys. ~~International Journal of~~*Int. J. Hydrogen Energy*~~,~~ **2007**~~.~~, *32*~~(16): p.~~, 3947~~–~~–3953.
15 Liu, X.-P~~., F.~~.; Cuevas, ~~L. J.~~F.; Jiang, ~~M.~~:.; Latroche, ~~Z. N.~~M.; Li, ~~and S. M.~~Z.; Wang, S. Improvement of the hydrogen storage properties of Ti–Cr–V–Fe BCC alloy by Ce addition. ~~Journal of~~*J. Alloys* ~~and Compounds,~~*Compd.* **2009**~~.~~, *476*~~(1–2): p.~~, 403~~–~~–407.
16 Yoo, J~~. H., G.~~.; Shim, ~~C. N.~~G.; Park, ~~W. B.~~C.; Kim, ~~and~~W.; Cho, S~~. W. Cho,~~. Influence of Mn or Mn plus Fe on the hydrogen storage properties of the Ti-Cr-V alloy. ~~International Journal of~~*Int. J. Hydrogen Energy*~~,~~ **2009**~~.~~, *34*~~(22): p.~~, 9116~~–~~–9121.
17 Okada, M., Kuriiwa, T., Tamura, T., Takamura, H., & Kamegawa, A. ~~(2002). *Journal of*~~*J. Alloys* ~~*and Compounds*(~~*Compd.* **2002**, *330*~~–~~–*332*~~),~~, 511~~–~~–516.
18 Liu, X.; Jiang, L.; Li, Z.; Huang, Z.; Wang, S. Improve plateau property of $Ti_{32}Cr_{46}V_{22}$ BCC alloy with heat treatment and Ce additive. *J. Alloys Compd.* **2009**, *471*, L36–L38.
19 Chen, X.; Yuan, Q.; Madigan, B.; Xue, W. Long-term corrosion behavior of martensitic steel welds in static molten Pb–17Li alloy at 550°C. *Corros. Sci.* **2015**, *96*, 178–185.
20 Chuang, H.J.; Huang, S.S.; Ma, C.Y.; Chan, S.L.I. Effect of annealing heat treatment on an atomized $AB_2$ hydrogen storage alloy. *J. Alloys Compd.* **1999**, *285*, 284–291.
21 Hang, Z.; Xiao, X.;Li, S.; Ge, H.; Chen, C.; Chen L. Influence of heat treatment on the microstructure and hydrogen storage properties of $Ti_{10}V_{77}Cr_6Fe_6Zr$ alloy. *J. Alloys Compd.* **2012**, *529*, 128–133.
22 Yu, X.B.; Wu, Z.; Xia, B.J.; Xu, N.X. A Ti-V-based bcc phase alloy for use as metal hydride electrode with high discharge capacity. *J. Chem. Phys.* **2004**, *121*, 987–990.

23 Young, K.; Ouchi, T.; Huang, B.; Nei, J. Structure, hydrogen storage, and electrochemical properties of body-centered-cubic $Ti_{40}V_{30}Cr_{15}Mn_{13}X_2$ alloys (*X* = B, Si, Mn, Ni, Zr, Nb, Mo, and La). *Batteries* **2015**, 1, 74–90.

24 Young, K.; Huang, B.; Regmi, R.K.; Lawes, G.; Liu, Y. Comparisons of metallic clusters imbedded in the surface oxide of $AB_2$, $AB_5$, and $A_2B_7$ alloy. *J. Alloys Compd.* **2010**, *506*, 831–840.

25 Young, K.; Ouchi, T.; Koch, J.; Fetcenko, M.A. Compositional optimization of vanadium-free hypo-stoichiometric $AB_2$ metal hydride alloy for Ni/MH battery application. *J. Alloys Compd.* **2012**, *510*, 97–106.

26 Young, K.; Ouchi, T.; Huang, B.; Fetcenko, M.A. Effects of B, Fe, Gd, Mg, and C on the structure, hydrogen storage, and electrochemical properties of vanadium-free $AB_2$ metal hydride alloy. *J. Alloys Compd.* **2012**, *511*, 242–250.

27 ASTM, Standard Practice for Calculation of Corrosion Rates and Related Information from Electrochemical Measurements, 1999, ASTM: West Conshohocken, United States.

28 Handzlik, P.; Fitzner, K. Corrosion resistance of Ti and Ti–Pd alloy in phosphate buffered saline solutions with and without $H_2O_2$ addition. *Tran. Nonfer. Met. Soc. China* **2013**, *23*, 866–875.

29 Young, K.; Nei, J. The current status of hydrogen storage alloy development for electrochemical application. *Materials* **2013**, *6*, 4574–4608.

30 ~~Sung Wook~~ Cho, ~~Chang Suck~~S.; Han, ~~Choong Nyeon~~C.; Park, ~~and Etsuo~~C.; Akiba~~, 'The~~ E. The Hydrogen Storage Characteristics of Ti–Cr–V ~~Alloys', *Journal of*~~ Alloys ~~*and Compounds*~~. *J. Alloys Compd.*, **1999**, *288* ~~(1999),~~, 294 ~~98~~ –298.

31 Cho, S.; Enoki, H.; Akiba, E. Effect of Fe addition on hydrogen storage characteristics of $Ti_{0.16}Zr_{0.05}Cr_{0.22}V_{0.57}$ alloy. *J. Alloys Compd.* **2000**, *307*, 304–310.

~~32~~32 Enomoto, M. The Cr-Ti-V system. *J. Phase Equilibria* **1992**, *13*, 195–200.

33 Dou, T.; Wu, Z.; Mao, J.; Xu, N. Application of commercial ferrovanadium to reduce cost of Ti–V-based BCC phase hydrogen storage alloys. *Mater. Sci. Eng. A* **2008**, *476*, 34–38.

~~33~~34 Santos, S.F.; Huot, J. Hydrogen storage in $TiCr_{1.2}(FeV)_x$ BCC solid solutions. *J. Alloys Compd.* **2009**, *472*, 247–251.

~~34~~35 Chen, N.; Li, R.; Zhu, Y.; Liu, Y.; Pan, H. Electrochemical hydrogenation and dehydrogenation mechanisms of the Ti–V base multiphase hydrogen storage electrode alloy. *Acta Metall. Sin.* **2004**, *40*, 1200–1204.

~~35~~36 Young, K.; Ouchi, T.; Nei, J.; Wang, L. Annealing effects on Laves phase-related body-centered-cubic solid solution metal hydride alloys. *J. Alloys Compd.* **2016**, *654*, 216–225.

~~36~~37 Cho, S.-W.; Enokib, E.; Akibab, E. Effect of Fe addition on hydrogen storage characteristics of $Ti_{0.16}$ $Zr_{0.05}$ $Cr_{0.22}$ $V_{0.57}$ alloy. *J. Alloys Compd.* **2000**, *307*, 304–310.

~~37~~38 Yoo, J.; Shim, G.; Cho, S.; Park, C. Effects of desorption temperature and substitution of Fe for Cr on the hydrogen storage properties of alloy. *Int. J. Hydrogen Energy* **2007**, *32*, 2977–2981.

~~38~~39 Dou, T.; Wu, Z.; Mao, J.; Xu, N. Application of commercial ferrovanadium to reduce cost of Ti–V-based BCC phase hydrogen storage alloys. *Mat. Sci. Engineer. A.* **2008,** *476*, 34–38.

~~39~~40 Itoh, H.; Arashima, H.; Kubo, K.; Kabutomori, T. The influence of microstructure on hydrogen absorption properties of Ti–Cr–V alloys. *J. Alloys Compd.* **2002**, *330*, 287–291.

~~40~~41 Towata, S.; Noritake, T.; Itoh, A.; Aoki, M.; Miwa, K. Effect of partial niobium and iron substitution on short-term cycle durability of hydrogen storage Ti–Cr–V alloys. *Int. J. Hydrogen Energy* **2013**, *38*, 3024–3029.

~~41~~42 Ashworth, M.A.; Davenport., A.J.; Ward, R.M.; Hamilton, H.G.C. Microstructure and corrosion of Pd-modified Ti alloys produced by powder metallurgy. *Corros. Sci.* **2010**, *52*, 2413–2421.

~~42~~43 Young, K.; Wong, D.F.; Nei, J. Effects of vanadium/nickel contents in Laves phase-related body-centered-cubic solid solution metal hydride alloys. Batteries **2015**, *1*, 34–53.

~~43~~44 Young, K.; Ouchi, T.; Nei, J.; wang, L. Annealing effects on Laves phase-related body-centered-cubic solid solution metal hydride alloys. J. Alloys Compd. **2016**, *654*, 216–225.

~~44~~45 Young, K.; Ouchi, T.; Meng, T.; Wong, D.F. Studies on the synergetic effects in multi-phase metal hydride alloys. Batteries **2016**, *2*, 15.

~~45~~46 Zhou, Y.; Chen, J.; Xu, Y.; Liu, Z. Effects of Cr, Ni and Cu on the Corrosion Behavior of Low Carbon Microalloying Steel in a $Cl^-$ Containing Environment. *J. Mater. Sci. Tech.* **2013**, *29*, 168–174.

~~46~~47 Kamimura, T.; Stratmann, M. The influence of chromium on the atmospheric corrosion of steel. *Corros. Sci.* **2001**, *43*, 429–447.

~~47~~48 Shih, C.; Shih, C.; Su, Y.; Su, L.H.L.; Chang, M.; Lin, S. Effect of surface oxide properties on corrosion resistance of 316L stainless steel for biomedical applications. *Corros. Sci.* **2004**, *46*, 427–441.

~~48~~49 Güleryüz, H.; H. Çimenoğlu. Effect of thermal oxidation on corrosion and corrosion–wear behaviour of a Ti–6Al–4V alloy. *Biomaterials* **2004**, *25*, 3325–3333.

~~49~~50 Shi, P.; Ng, W.F.; Wong, M.H.; Cheng, F.T. Improvement of corrosion resistance of pure magnesium in Hanks' solution by microarc oxidation with sol–gel $TiO_2$ sealing. *J. Alloys Compd.* **2009**, *469*, 286–292.

~~50~~51 Iba, H; Akiba, E. The relation between microstructure and hydrogen absorbing property in Laves phase-solid solution multiphase alloys. *J. Alloys Compd.* **1995**, *231*, 508–512.

~~51~~52. Tsukahara, M.; Takahashi, K.; Mishima, T.; Isomura, A.; Sakai, T. V-based solid solution alloys with Laves phase network: hydrogen absorption properties and microstructure. *J. Alloys Compd.* **1996**, *236*, 151–155.

© 2016 by the authors; licensee MDPI, Basel, Switzerland. This article is an open access article distributed under the terms and conditions of the Creative Commons by Attribution (CC-BY) license (http://creativecommons.org/licenses/by/4.0/).